Journal of Fluids and Structures 100 (2021) 103170

Contents lists available at ScienceDirect

Journal of Fluids and Structures

journal homepage: www.elsevier.com/locate/jfs

Pivot location and mass ratio effects on flow-induced vibration of a fully passive flapping foil

Zhuo Wang [a], Lin Du [a,*], Jisheng Zhao [b], Mark C. Thompson [b], Xiaofeng Sun [a]

[a] School of Energy and Power Engineering, Beihang University, Beijing, 100191, China
[b] Fluids Laboratory for Aeronautical and Industrial Research (FLAIR), Department of Mechanical and Aerospace Engineering, Monash University, Clayton, Victoria 3800, Australia

ARTICLE INFO

Article history:
Received 22 June 2020
Received in revised form 27 September 2020
Accepted 21 October 2020
Available online xxxx

Keywords:
Eccentricity
Mass ratio
Fluid–structure interaction

ABSTRACT

This paper reports on an extensive numerical investigation of the effects of pivot location and mass ratio (m^* = solid/fluid mass) on flow-induced vibration (FIV) of a foil undergoing fully passive two-degree-of-freedom (2-DOF) plunging and pitching motion in a two-dimensional free-stream flow. Here, the normalised pivot location is defined by $x = x_p/c$, with c the foil length and x_p the distance to the foil leading edge. A comprehensive set of numerical simulations were conducted employing an Immersed Boundary Method at a Reynolds number of 400. By analysing the FIV dynamics for three selected mass ratios, $m^* = 5$, 20 and 200, at two pivot locations, $x = 0.35$ and 0.50, it is found that there are two types (type-I and type-II) of FIV responses, one is primarily a driven static instability while the other is strongly associated with vortex shedding. Interestingly, for $x = 0.50$, which is close to the mass centre, increasing the mass ratio can favour suppression of the chaotic response. Importantly, it is shown that there exists a critical mass ratio, above which the foil oscillations are suddenly suppressed. The findings indicate that the combined effects of eccentricity and mass ratio on the foil dynamics can be profound.

1. Introduction

Flow-induced vibration (FIV) is a vibration phenomenon resulting from the coupled interaction between the structure and the surrounding fluid flow (also known as fluid–structure interaction). FIV finds its importance in a broad range of engineering applications. For example, undesirable effects of FIV may lead to structural damage or complete failure in heat exchanger tubes of nuclear plants, offshore oil risers, high-rise buildings and bridges, and they may also threaten the structural fatigue life and safety of aero-engine blades and aircraft. In contrast to these detrimental effects, on the other hand, FIV has recently been demonstrated as a potential source of renewable energy extracted through harnessing significant structural oscillations, e.g. vortex-induced vibration (VIV) of cylinders (see Soti et al., 2018), and passive motions of flapping foils (see Wang et al., 2017). Over the last few decades, both practical and fundamental perspectives of the problem have motivated a large body of studies that aim to better understand the fluid–structure mechanisms, predict structural vibration characteristics, and develop vibration control approaches. Comprehensive reviews on the subject of FIV, predominantly for bluff bodies, can be found in the articles of Griffin et al. (1973), Bearman (1984), Sarpkaya (2004),

* Corresponding author.
E-mail address: lindu@buaa.edu.cn (L. Du).

https://doi.org/10.1016/j.jfluidstructs.2020.103170
0889-9746/

Williamson and Govardhan (2004) and Gabbai and Benaroya (2005), and the books of Blevins (1990), Naudascher and Rockwell (2005) and Paidoussis et al. (2010).

Compared to bluff bodies, however, the fundamentals of FIV of flapping foils has received much less attention. The majority of early studies of flapping foils in a fluid flow have focused on determining the energy extraction performance; the reader is referred to the recent reviews on this topic by Xiao and Zhu (2014) and Young et al. (2014). For example, McKinney and DeLaurier (1981), inspired by the wings of birds, performed pioneering experiments to investigate energy extraction from a sinusoidally-driven wing. Since then, ongoing research has been conducted on the energy-harvesting performance of foils with 2-DOF motions of plunging and pitching. In general, flapping foils with 2-DOF motions are classified into three categories depending on their operational modes (see Xiao and Zhu, 2014; Young et al., 2014): (i) *fully forced systems* that have both plunging and pitching motions fully prescribed, e.g. (see Kinsey and Dumas, 2008; Platzer et al., 2010; Ashraf et al., 2011; Zhu, 2012); (ii) *semi-passive systems* that usually have prescribed motion in one DOF but allow free motion in the other e.g. (see Deng et al., 2015; Boudreau et al., 2019a,b); and (iii) *fully passive systems* that have both plunging and pitching motions free, fully determined by the fluid–structure interaction (see Wang et al., 2017; Veilleux and Dumas, 2017; Boudreau et al., 2018, 2020; Duarte et al., 2019).

More recently, Wang et al. (2017, 2020) conducted low-Reynolds-number ($Re = 400$) numerical simulations to investigate the fundamentals of the FIV response of a foil undergoing fully passive 2-DOF motions of plunging and pitching, as a function of reduced velocity and pivot location in a two-dimensional free-stream flow. Here, the reduced velocity is defined by $U^* = U/(f_n c)$, where U is the free-stream velocity, c is the foil chord length, and f_n is the natural frequency of both plunging and pitching motions (set equal); the pivot location (from the foil leading edge) is denoted by x_p, and its normalised form is given by $x = x_p/c$; and the Reynolds number is defined by $Re = Uc/\nu$, with ν being the kinematic viscosity of the fluid. Wang et al. (2017) showed the dependence of the FIV response on the reduced velocity and the pivot location over the ranges of $0 < U^* \leqslant 7$ and $0 \leqslant x \leqslant 1$, and also demonstrated complex nonlinear dynamics that could lead to very large structural vibrations. Furthermore, through detailed analyses of the dynamics and wake states over an extended and finer $x - U^*$ space ($0 < U^* \leqslant 10$ and $0 \leqslant x \leqslant 1$), Wang et al. (2020) identified a variety of FIV response regimes, including four regions that exhibited synchronisation or near-synchronisation responses and four transition regimes that were associated with intermittent, switching or chaotic responses. These two studies have indicated that the eccentricity effect due to the pivot location has an impact on the coupling between the 2-DOF motions and thus the FIV dynamics.

On the other hand, the mass ratio, defined as the ratio of the total mass of a vibrating structure to the mass of displaced fluid, has been shown to play a significant role affecting the FIV dynamics and response regimes of bluff bodies, such as circular cylinders (see Feng, 1968; Khalak and Williamson, 1996; Govardhan and Williamson, 2000, 2002; Jauvtis and Williamson, 2004), and square cylinders (see Nemes et al., 2012; Zhao et al., 2019). It has been demonstrated by Wang et al. (2017, 2020) that the nonlinear coupling between the plunging and pitching motions of a foil is strongly associated with the pitching inertial moment that is dependent on system mass and the offset of the pivot location from the centre of mass. Thus, one would expect that the mass ratio can also have a impact on the dynamics of a fully passive foil. To date, however, the effects of eccentricity and mass ratio on a flapping foil have been largely unknown and unexplored. Thus, built upon the previous studies of Wang et al. (2017, 2020), this paper aims to investigate these effects by examining the FIV response and dynamics of a foil as a function of reduced velocity at various pivot locations, specifically focusing on a wide range of mass ratios.

The rest of this paper is organised as follows: the fluid–structure system modelling and the numerical method are described in Section 2. It should be noted that validation studies of the present numerical method for the same physical and computational setup are provided through the previous studies of Du et al. (2016a,b), Wang et al. (2017, 2020), and so are not be repeated in this paper. In order to highlight the effects of eccentricity and mass ratio, results and discussion are presented in Sections 3.1–3.5 in sequence, where the FIV dynamics are characterised as a function of the reduced velocity, mass ratio and pivot location. Finally, conclusions are drawn in Section 4.

2. Numerical approach

The numerical method used here is adopted from Du et al. (2016a,b) and Wang et al. (2017, 2020). The fluid–structure system consists of an elastically mounted NACA0012 foil with two degrees of freedom, namely plunge and pitch, in a free-stream flow. Fig. 1 presents a schematic (top view) of the fluid–structure system, where key parameters are illustrated. Here, the fluid density, dynamic viscosity and incoming flow velocity are denoted by ρ, μ and U, respectively; the foil is free to undergo plunging (or heaving) motion transverse to the incoming flow and pitching motion about the axis perpendicular to the direction of free-stream flow and the plunging axis; the instantaneous displacement in plunge is denoted by h, and its normalised form is defined by $h^* = h/c$; the displacement in pitch is denoted by θ, which is measured in radians. The instantaneous transverse lift and pitching moment are denoted by F_h and M_θ, respectively. The structural stiffnesses in plunge and pitch are specified by k_h and k_θ, respectively, while the corresponding damping factors are c_h and c_θ, respectively. Note that both c_h and c_θ are set to zero here to simplify the system and examine the least damped case. The distance from the leading edge to the pivot location is denoted by x_p, and its dimensionless form (x) is given by

$$x = x_p/c. \tag{1}$$

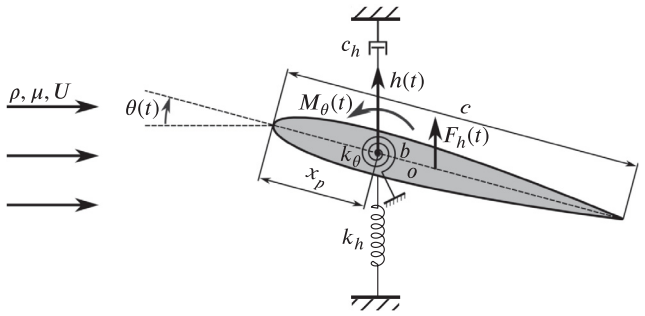

Fig. 1. Schematic (top view) of the fluid–structure system considered: a NACA0012 foil allowed to undergo 2-DOF fully passive plunging and pitching motions.

The elastically mounted foil is considered as a linear mass–spring system, and its plunge and pitch motions are governed by the second-order oscillator equations (2):

$$\begin{aligned} &m\ddot{h} + c_h\dot{h} + k_h h - mb\cos\theta\cdot\ddot{\theta} + mb\sin\theta\cdot\dot{\theta}^2 = F_h \\ &I_\theta\ddot{\theta} + c_\theta\dot{\theta} + k_\theta\theta - mb\cos\theta\cdot\ddot{h} = M_\theta, \end{aligned} \tag{2}$$

where m and I_θ denote the mass and the (second moment of) inertia in pitch of the foil, respectively. The eccentricity arising from the coupling of the plunge and pitch motions is evaluated by the product of mb in Eq. (2). The mass ratio, defined as the ratio of the foil mass per unit length to the displaced fluid mass, is given by Eq. (3):

$$m^* = \frac{m}{\rho S} \tag{3}$$

where S is the area of the cross section of the foil. Also, b denotes the distance between the pivot location and the mass centre (the point o in Fig. 1). The reduced velocity is given by $U^* = U/(f_n c)$, noting that the natural frequencies of the 2-DOF motions are set to be equal, $f_n = \sqrt{k_h/m}/2\pi = \sqrt{k_\theta/I_\theta}/2\pi$. In the present study, the variation of U^* is achieved by changing the spring stiffness. The fluid forcing terms, F_h and M_θ, are obtained through solving the governing equations of fluids. The fourth-order Runge–Kutta method is applied to obtain the numerical solution for Eq. (2). The dimensionless coefficients of F_h and M_θ are given by Eqs. (4) and (5), respectively,

$$C_h = \frac{F_h}{\frac{1}{2}\rho U^2 c} \tag{4}$$

$$C_m = \frac{M_\theta}{\frac{1}{2}\rho U^2 c^2}. \tag{5}$$

The dimensionless coefficients of inertial forces due to the coupling effect of the 2-DOF motions are given by Eqs. (6)–(8):

$$C_{Ih}^A = \frac{mb\cos\theta\cdot\ddot{\theta}}{\frac{1}{2}\rho U^2 c} \tag{6}$$

$$C_{Ih}^C = -\frac{mb\sin\theta\cdot\dot{\theta}^2}{\frac{1}{2}\rho U^2 c} \tag{7}$$

$$C_{Im}^A = -\frac{mb\cos\cdot\ddot{h}}{\frac{1}{2}\rho U^2 c^2}, \tag{8}$$

where C_{Ih}^A represents the inertial force coefficient in plunge induced by the acceleration of pitch motion (or rotation), while C_{Ih}^C is contributed by the centrifugal force of pitch motion, and C_{Im}^A represents the inertial moment coefficient induced by the acceleration of plunge motion. To estimate the relative magnitudes of the inertial forces and the fluid forces, the ratios of the root-mean-square (rms) values of the coefficients of the inertial forces and the fluid forces are calculated by Eqs. (9)–(11):

$$r_{Ih}^A = \frac{\mathrm{rms}(C_{Ih}^A)}{\mathrm{rms}(C_h)} \tag{9}$$

$$r_{Ih}^C = \frac{\mathrm{rms}(C_{Ih}^C)}{\mathrm{rms}(C_h)} \tag{10}$$

$$r_{I\theta} = \frac{\mathrm{rms}(C_{Im}^A)}{\mathrm{rms}(C_m)}. \tag{11}$$

The flow dynamics is solved by employing a two-dimensional incompressible Navier–Stokes solver. Detailed descriptions of the numerical method can be found in previous studies of Du et al. (2016a,b) and Wang et al. (2017) so only a brief outline is given here.

The continuity and momentum equations are written in dimensionless form as

$$\begin{aligned} &\nabla \cdot \vec{V} = 0, \\ &\frac{\partial \vec{V}}{\partial t} + (\vec{V} \cdot \nabla)\vec{V} = \vec{F} - \nabla p + \frac{1}{Re}(\nabla \cdot \nabla)\vec{V}, \end{aligned} \tag{12}$$

where $\vec{V} = (u, v)$ denotes the two-component flow velocity in the streamwise (u) and cross-flow (v) directions. The body force is denoted by $\vec{F}$. The fluid pressure is denoted by p. The Reynolds number is denoted by Re, which is set to be 400 in the present study.

To characterise the interaction between the fluid and the boundary, $\vec{F} = (F_x, F_y)$ is calculated using an immersed boundary (IB) method originally introduced by Peskin (1972, 1977). For the no-slip wall boundary condition, it can be treated as a process of negative feedback:

$$\vec{f}(x_k, y_k, t) = \alpha \int_0^t [\vec{v}_f(x_k, y_k, t') - \vec{v}_s(x_k, y_k, t')]\mathrm{d}t' + \beta[\vec{v}_f(x_k, y_k, t) - \vec{v}_s(x_k, y_k, t)], \tag{13}$$

where (x_k, y_k) denotes the coordinates of the kth surface element on the solid boundary; $\vec{v}_f$ and $\vec{v}_s$ denote the velocity of the fluid and the solid body at the kth surface element, respectively; α and β are feedback factors, noting that they should be chosen carefully to avoid a sensitive response of feedback. In the present study, $\alpha = \alpha_0/\Delta t$ with $\alpha_0 = 2.0$, and β is set to zero. In order to solve the flow equations, the body force constructed in the Lagrangian form is converted to the Euler domain using the Dirac delta function:

$$\vec{F}(x, y, t) = \int_\Gamma \vec{f}(x_k, y_k, t)\delta(x - x_k)\delta(y - y_k)\mathrm{d}s, \tag{14}$$

where (x, y) represents a point in the Cartesian coordinates and Γ depicts the solid boundary. The Dirac delta function is further approximated numerically following the method proposed by Peskin (2002): the singular Dirac function is replaced by a continuous but segmented function:

$$\Phi_r = \begin{cases} 0 & |r| \geqslant 2 \\ (5 - 2|r| - \sqrt{-7 + 12|r| - 4r^2})/8 & 1 \leqslant |r| \leqslant 2 \\ (3 - 2|r| + \sqrt{1 + 4|r| - 4r^2})/8 & 0 \leqslant |r| \leqslant 1, \end{cases} \tag{15}$$

where $r = \Delta x/\Delta h$, with Δx the distance between the boundary surface element and the nearest grid point in the fluid domain, and Δh the mesh width in the calculations. Validation studies can be found in Du et al. (2016a,b) and Wang et al. (2017, 2020).

3. Results and discussion

To show the combined effect of eccentricity and mass ratio for a foil undergoing fully passive 2-DOF oscillations, this section is organised as follows. Section 3.1 presents the dynamic response as a function of reduced velocity, for a mass ratio of $m^* = 5$ with the pivot location fixed at $x = 0.5$, including the oscillation amplitude responses, fluid forces, and frequency power spectrum density (PSD) contours. It should be noted that this pivot location is chosen to be close to the mass centre, to minimise the *eccentricity* effect. Thus, the corresponding results can provide a benchmark for further discussions. The mass ratio effect at the same pivot location is then demonstrated in Section 3.2, by examining results at higher mass ratios, i.e. $m^* = 20$ and 200. In Section 3.3, the effects of eccentricity and mass ratio are further discussed through the FIV responses at a different pivot location $x = 0.35$, a significant offset from the mass centre. To evaluate the detailed effects of these parameters further, FIV responses as a function as m^* and x are presented in Section 3.4 and Section 3.5, respectively.

3.1. Responses with $m^* = 5$ at fixed $x = 0.50$

3.1.1. Amplitudes and frequencies

Fig. 2 shows the mean of the top 10% amplitudes (A^{10}) of the normalised displacements in plunge (A_h) and pitch (A_θ), together with the root-mean-square (r.m.s.) coefficients of the transverse lift (C_h^{rms}), and pitching moment (C_m^{rms}), as a function of U^*, for three different mass ratios, $m^* = 5$, 20 and 200. The corresponding frequency PSD contours are shown in Fig. 3.

For $m^* = 5$ in Fig. 2(*a*), three response regimes, demarcated by vertical lines, covering the ranges $1.63 \leqslant U^* \leqslant 6.90$, $7.21 \leqslant U^* \leqslant 7.83$ and $8.14 \leqslant U^* \leqslant 20.0$, can be identified based on the dynamic characteristics. In the first regime, the 2-DOF oscillations, after excitement at $U^* = 1.63$, develop rapidly with increasing U^*. Local amplitude peaks of $(A_h^{10}, A_\theta^{10}) = (1.75, 2.50)$ are observed at $U^* = 5.35$, which are followed by a kink prior to an increasing trend, with U^*

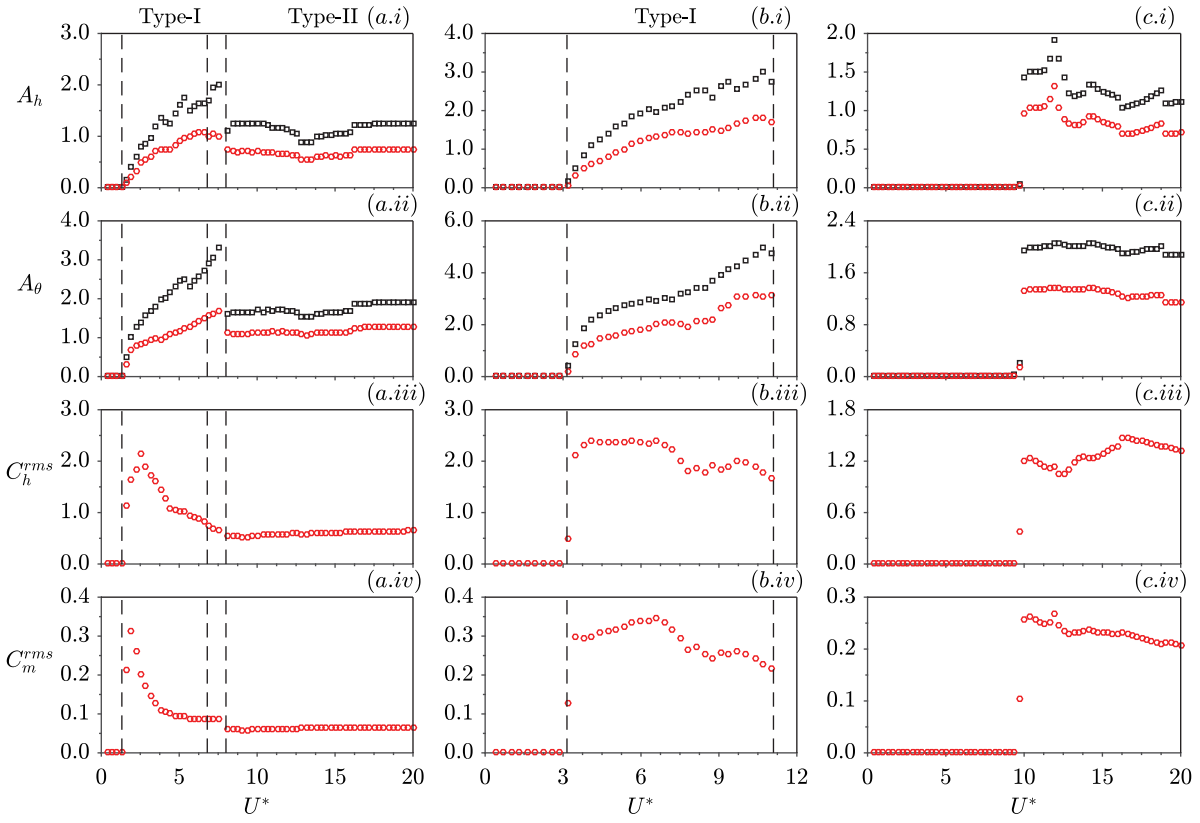

Fig. 2. The normalised amplitude responses of plunging (h^*) and pitching (θ) vibrations, the coefficients of the transverse lift (C_h) and pitching moment (C_m), in column (a) $m^* = 5$, (b) $m^* = 20$ and (c) $m^* = 200$, as a function of U^*, with fixed $x = 0.50$. The squares in black and the circles in red denote the mean top 10% (A^{10}) and the root-mean-square (A^{rms}) oscillation amplitudes, respectively.

continuing until the end of the regime marked by a sudden drop in both A_h^{10} and A_θ^{10} responses at $U^* = 6.90$. As can be seen from the normalised frequency PSD plots in Fig. 3(a), the dominant oscillation frequencies of the oscillations and fluid forcing components are found to be fairly stable at $f^* \approx 0.45$ (close to half of the natural frequency) over most of this regime. According to Dowell (2015), the FIV response of a 2-DOF fully passive foil can be characterised by two mechanisms in the linear range: static instability (or divergence), and dynamic instability (or flutter). The mechanism of static instability is that the restoring moment provided by the elastic support in pitch cannot balance the pitching moment applied by the flow, and the foil is thereby forced to rotate. Based on their experimental results, Boudreau et al. (2018) suggested that the oscillations of a 2-DOF fully passive foil were driven by this static instability. This can also be applied to explain the occurrence of the first regime in the present study. Further evidence for divergence instability will be provided in Section 3.5.

To demonstrate the dynamics in the first regime of the $m^* = 5$ case, sample time traces at $U^* = 2.87$ and 3.80, as representatives of the synchronisation and desynchronisation responses, are shown in Figs. 4(a, b), respectively. These time traces display that the highly periodic oscillations are modulated by harmonics, especially the 3rd harmonic, as clearly revealed by the corresponding frequency contours in Fig. 3(a). In an experimental study of transverse FIV of a square cylinder, Zhao et al. (2014) found that profound harmonic synchronisation responses could be attributed to a combined effect of galloping and vortex-induced vibration (VIV), where the dominant galloping frequency and the vortex-shedding frequency were of odd-integer ratios, e.g. 1:3 and 1:5. The high-order harmonics in these synchronisation responses were well related to the vortex shedding process, while the dominant oscillation frequency was related to the galloping frequency. The wake pattern associated with the synchronisation response in the type-I regime is presented in Section 3.1.2. Harmonic synchronisations can often result in an amplitude growth with increasing reduced velocity, as can be seen in the present A_h^{10} and A_θ^{10} responses. In contrast, when U^* is increased to 3.80, as shown in Fig. 4(b), and the time traces can maintain their periodicity for several cycles and then suddenly become irregular, e.g. $\tau = 10$ in Fig. 4(b). Correspondingly, the frequency contours in Fig. 3(a) also see obvious broadband noise, which is indicative of desynchronisation. As detailed by Wang et al. (2020), such a variation of the time profiles was associated with intermittent switching of wake patterns.

The second regime of $m^* = 5$ covers the range of $7.21 \leqslant U^* \leqslant 7.83$, which is characterised as a narrow transition regime featuring chaotic and irregular responses. The oscillation amplitudes reach their maximums in this regime,

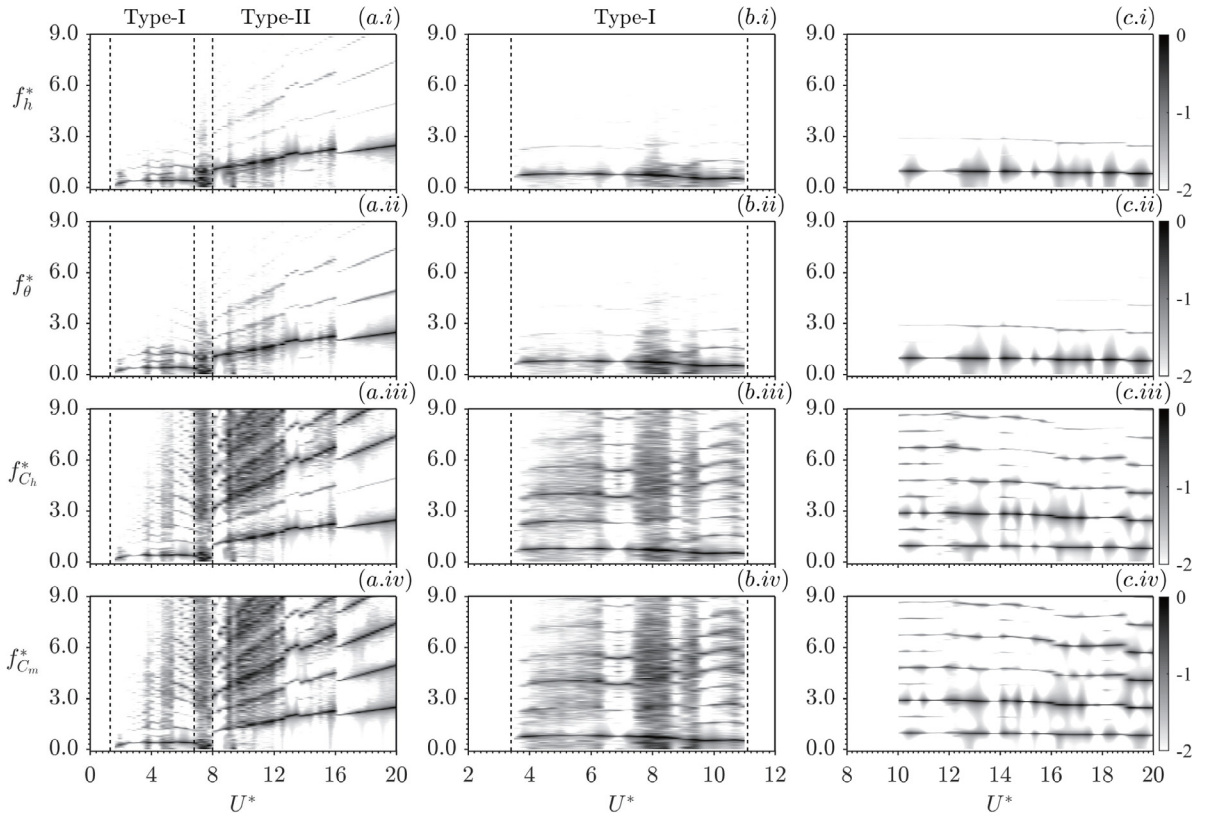

Fig. 3. The logarithmic-scale frequency power spectrum density contours of h^*, θ, C_h and C_m at (a) $m^* = 5$, (b) $m^* = 20$ and (c) $m^* = 200$, as a function of U^*, with fixed $x = 0.50$. The frequency components are normalised by f_n.

i.e., $(A_h^{10}, A_\theta^{10}) = (2.03, 3.33)$ at $U^* = 7.52$. Representative time traces at $U^* = 7.52$ are shown in Fig. 4(*c*). It can be seen that both the plunge and pitch oscillation equilibrium positions switch stochastically between two values, which are symmetrical about the initial neutral positions ($h^* = 0$ and $\theta = 0$), indicating a chaotic characteristic. The corresponding frequency contours for the second regime shown in Fig. 3(*a*) also display obvious broadband noise. Such chaotic responses were also reported both in previous numerical and experimental investigations (see Duarte et al., 2019; Wang et al., 2020), which could be attributed to mode competition between two states, as chaos has been observed in similar situations in various fluid–structure systems (see Crawford and Knobloch, 1991; Leontini and Thompson, 2013; Zhao et al., 2018b). However, when the mass ratio is increased to 200, the switching behaviour of equilibrium positions disappear, suggesting that such a behaviour seemingly occurs only at low mass ratio, as will be discussed below.

The third regime is embedded in the reduced velocity range of $8.14 \leqslant U^* \leqslant 20.0$, where the magnitudes of the foil oscillations and fluid forces exhibit only slight fluctuations as U^* varies, while the dominant frequencies and their harmonics tend to follow a linear relationship with U^*. It should be noted that broadband noise is still identifiable over the range of $8.50 \leqslant U^* \leqslant 12.5$; however, as U^* is further increased, all frequency components gradually become clearer. To demonstrate the dynamics, sample time traces at $U^* = 15.04$ are presented in Fig. 4(*d*), showing a periodic state. The frequency contours as well as the sample time-trace profiles suggest that the third regime can be considered as a near-synchronisation regime. Note that in this regime non-zero equilibrium positions are consistently observed for both plunge and pitch oscillations, whereas in the first regime the equilibrium positions are found to remain constantly close to zero.

Wang et al. (2020) studied the flow-induced vibrations of a 2-DOF airfoil with $m^* = 2.0$ over a wide (x, U^*) parameter space, where four synchronous or nearly synchronous regimes were identified, namely S-I, S-II, S-III and S-IV. The three regimes of $m^* = 5$ at fixed $x = 0.50$ correspond to regimes S-I, T-II and S-III in Wang et al. (2020), respectively, which occur in sequence as U^* is increased in the present study. More detailed analyses for the response characteristics of $m^* = 5.0$ at $x = 0.5$, including the dynamics and wake patterns, can be referred to the corresponding discussion in Wang et al. (2020). Despite comparison against a lower mass ratio of $m^* = 2$ in their study, highly similar characteristics would be expected for the present $m^* = 5$ case. Rather than repeating similar results and discussion as in Wang et al. (2020), the present study focuses on the effects of eccentricity and mass ratio, and thereby the case of $m^* = 5$ will be considered as a baseline case to reveal the mass ratio effect at this pivot location.

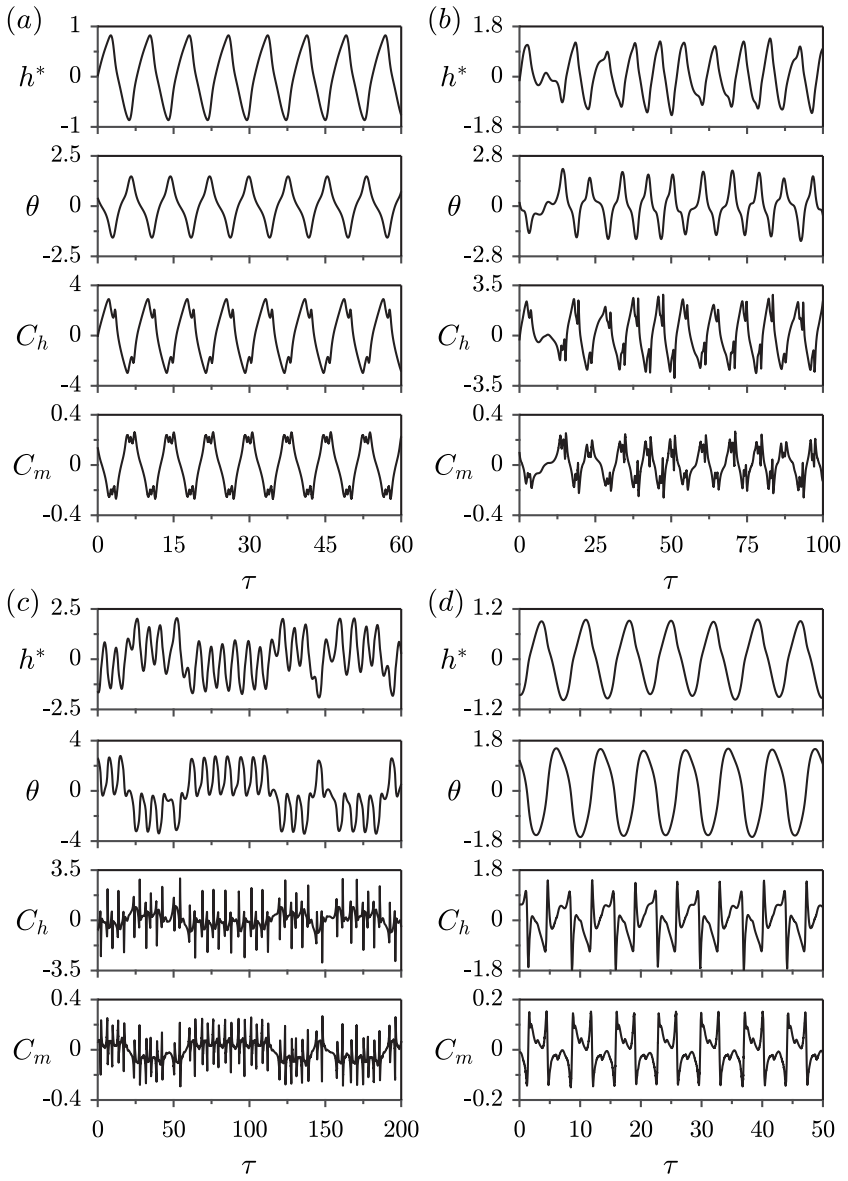

Fig. 4. Time traces of the responses, including the displacements in plunge (h^*) and pitch (θ), the coefficients of the transverse lift (C_h) and pitching moment (C_m) at (a) $U^* = 2.87$, (b) $U^* = 3.80$, (c) $U^* = 7.52$ and (d) $U^* = 15.04$.

Furthermore, it will be demonstrated in the following subsections — as the pivot location or mass ratio is varied, the dynamic characteristics of the first and third regimes can also be widely observed. For the convenience of the discussion, the first and third regimes are herein referred to as type-I and type-II regimes, respectively. The type-I regime can be characterised by a general increasing trend in the amplitude response with increasing U^*, while the dominant oscillation frequencies are independent of U^* over some discrete U^* ranges, which are similar to the characteristics of response associated with the transverse galloping of 1-DOF FIV systems (see Zhao et al., 2018a). For the type-II regime, the amplitude responses only show minor variations through the regime, while the frequency components follow a linear growth trend with increasing U^*, as dominated by the vortex shedding process.

3.1.2. Wake patterns associated with synchronisations

To further demonstrate the dynamic characteristics, typical wake patterns at $(x, m^*) = (0.5, 5)$, as well as their dependence on the oscillation amplitude and synchronisation state, will be discussed in this subsection. Wang et al. (2020) presented a wake map in an $x - U^*$ parameter space for $m^* = 2$, showing a variety of wake modes and intermittent switching behaviours. Stable wake modes associated with synchronisation responses are also of great concern in the

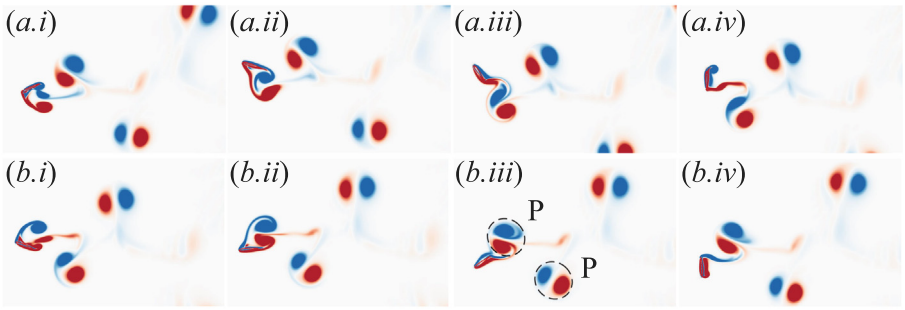

Fig. 5. A 2P wake pattern, which consists of two pairs (P) of opposite-signed vortices shed per foil oscillation cycle, is observed at $(x, m^*, U^*) = (0.5, 5, 3.18)$.

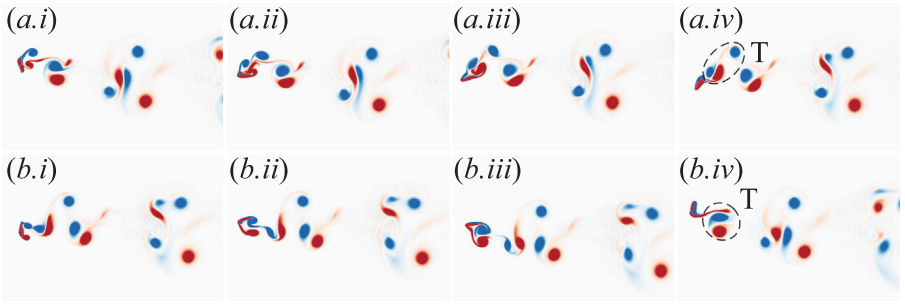

Fig. 6. A 2T wake pattern, which consists of two triplets (T) of vortices shed per foil oscillation cycle, is observed at $(x, m^*, U^*) = (0.5, 5, 4.11)$.

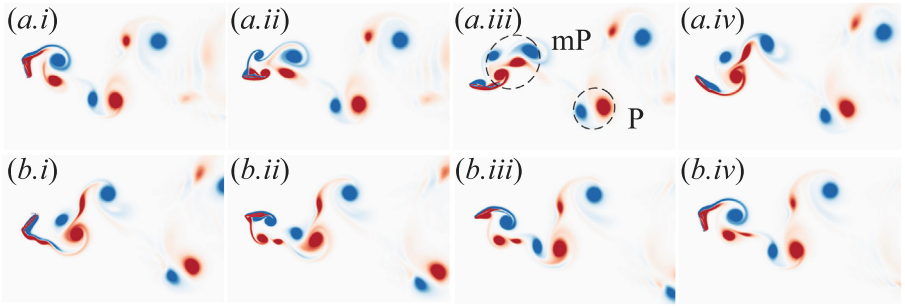

Fig. 7. A mP+P wake pattern, which consists of multiple pairs (mP) of vortices shed in one half foil oscillation cycle plus another pair (P) of vortices shed in the other half cycle, is observed at $(x, m^*, U^*) = (0.5, 5, 15.04)$.

present work. As can be seen from 3(a), a synchronisation regime ($2.4 \leqslant U^* \leqslant 3.3$) is observed in the type-I regime, where harmonic components appear to be clear in the frequency PSD contours. The corresponding wake mode at $U^* = 3.18$, as a representative for this synchronisation regime, is shown in Fig. 5. During one half oscillation cycle, a pair (P) of vortices are shed into the wake and the following half cycle repeats the pattern (with opposite-signed vortices). Following the nomenclature of Williamson and Roshko (1988) and Morse and Williamson (2009), this wake mode is termed as 2P. As shown in Section 3.1.1, the foil response at $U^* = 3.18$, which displays a galloping characteristic, is dominated by the first harmonic (as the fundamental harmonic). The shedding of the 2P vortices induces multiple loading excitations on the foil during one oscillation cycle, thus giving rise to the higher-order harmonics as seen in the corresponding frequency PSD contours in Fig. 3(a). As U^* is further increased, synchronisation responses (over the range of $4.0 \leq U^* \leq 4.6$) are observed again within the type-I regime. As can be seen from Fig. 6, a triple (T) of vortices is shed during one half oscillation cycle at $U^* = 4.10$ and this wake mode is thus named 2T pattern (see Williamson and Roshko, 1988; Morse and Williamson, 2009). A comparison between the responses for $U^* = 3.18$ and 4.10 shows that, with the increase in the oscillation amplitudes in the type-I regime, more vortices will shed during one oscillation cycle, and correspondingly high-order harmonic components are also found to be obvious in the fluid forces as shown by Fig. 3($a.iii - v$). This trend is similar to that observed in transverse galloping responses of single-DOF bluff bodies (e.g. Zhao et al., 2014, 2018a). For the desynchronisation responses in the type-I regime, the vortex shedding is found to be unstable, which may switch

intermittently between different wake modes observed in the synchronisation response in the type-I regime. Detailed discussion on switching behaviours of wake modes can be found in Wang et al. (2020).

Fig. 7 illustrates a mP+P wake mode at $U^* = 15.04$ for $(x, m^*) = (0.5, 5)$, as a representative for the corresponding type-II regime. This wake mode consists of multiple pairs of vortices shed in one half cycle plus another paired vortices shed in another half cycle. Wang et al. (2020) reported that, in some synchronisation responses at high U^* values, multiple pairs (two or three) of vortices are shed one half cycle and this mode was referred to as multiple P (mP). Thus, wake pattern in Fig. 7 is named mP+P. Note that in the case of $m^* = 2$ in Wang et al. (2020), an mP mode was encountered when the foil oscillated around a non-zero equilibrium position both in plunge and pitch. Similarly, this wake mode is observed in the type-II regime at $x = 0.5$ and $m^* = 5$ in the present study. Hence, the occurrence of the mP mode might be well related to the variation of the equilibrium position in a 2-DOF foil system. Multiple pairs of vortices can result in multiple loading excitations on the foil during one oscillation cycle and the higher-order harmonics thus play a significant role in the fluid forces, as shown in Fig. 3($a.iii$–v).

3.2. Responses with higher mass ratios at $x = 0.50$

The FIV responses of two higher mass ratio cases, $m^* = 20$ and 200, are examined in this subsection. The amplitude responses (A_h, A_θ) and variations of the fluid forcing coefficients (C_h^{rms} and C_m^{rms}) for these two mass ratios are plotted as a function of U^* in Fig. 2(b, c), and the corresponding frequency PSD contours are shown in Fig. 3(b, c). As can be seen, the reduced velocities of onset for significant foil oscillations are found to be $U^* = 1.63$, 3.18 and 9.69 for $m^* = 5$, 20 and 200, respectively. Perhaps, it is not surprising that the onset of significant oscillations tends to occur at a higher U^* as m^* is increased, as demonstrated in previous studies on 1-DOF transverse FIV of bluff bodies (e.g. Khalak and Williamson, 1996; Govardhan and Williamson, 2002; Zhao et al., 2019).

For $m^* = 20$, the investigation is limited to the range of $0.0 < U^* \leqslant 11.01$. This is simply because reliable results become unavailable beyond $U^* = 11.01$, due to numerical divergence errors occurring in this m^* case. As shown in Fig. 2(b), the varying trends of C_h^{rms} and C_m^{rms} for $m^* = 20$ exhibit a type-I response, similar to that observed in the case of $m^* = 5$ in Fig. 2(a), where both C_h^{rms} and C_m^{rms} tend to increase rapidly with U^*. However, the present case sees much larger amplitudes, i.e., $(A_h^{10}, A_\theta^{10} = 3.00, 4.95)$ at $U^* = 10.7$. On the other hand, type-I frequency response can also be seen in the PSD contours in Fig. 3(b), where the dominant frequencies of the 2-DOF oscillations remains fairly constant (i.e. $f_h^* \simeq f_\theta^* \approx 0.80$) for U^* up to 8.0 prior to a slight decrease for the higher U^* range tested.

It should be noted that in addition to the dominant frequency, there are "odd" harmonics (i.e. at the 3rd and 5$^{\text{th}}$) existing over most of the regime. Specifically, these harmonics are clearly observable over three U^* ranges: $6.28 \leqslant U^* \leqslant 7.52$, $8.60 \leqslant U^* \leqslant 9.00$ and $9.69 \leqslant U^* \leqslant 10.30$, suggesting that harmonic synchronisation is encountered in these ranges. On the contrary, mild broadband noise is presented in the frequency PSD contours at other U^* locations. However, chaotic transition responses, as well as the type-II regime seen in the high U^* range for $m^* = 5$, have not been observed at $m^* = 20$. This indicates that the foil oscillations are strongly influenced by the mass ratio – a higher mass ratio can result in larger inertial forces, which may help suppress the chaotic response where the eccentricity effect is weak (i.e., when the pivot location is close to the mass centre). Although oscillations with stable amplitudes have not been obtained for $U^* > 11.01$, it could still be inferred from the oscillation amplitude evolutions at the initial stage of simulations that higher oscillation amplitudes might be encountered for higher U^* values. This feature is similar to that commonly seen in transverse galloping of 1-DOF FIV systems (see Zhao et al., 2014; Seyed-Aghazadeh et al., 2017; Zhao et al., 2018a).

As m^* is further increased to 200, as expected, a significant reduction is observed in the overall amplitude responses. As shown in Fig. 2(c), both A_h^{10} and A_θ^{10} for $m^* = 200$ experience a sudden jump from very small initial magnitudes to $(A_h^{10}, A_\theta^{10}) = (1.44, 1.95)$ at $U^* = 10.0$. For higher reduced velocities, A_h^{10} fluctuates largely but still tends to decrease with increasing U^*, while, on the other hand, A_θ^{10} decreases slightly. This response is distinctly different from the cases of $m^* = 5$ and 20.

To further examine the FIV responses for $m^* = 200$, the corresponding frequency PSD contours are plotted in Fig. 3(c). Synchronisation responses seem to dominate the whole U^* range at $m^* = 200$, as evidenced by the appearance of clear harmonics with little noise. The dominant frequencies are found to be close to unity for all cases at $m^* = 200$, similar to the type-I regimes observed for lower mass ratios. However, the A_h and A_θ responses in the type-I regimes for $m^* = 5$ and 20 are found to increase with U^*, while at $m^* = 200$ the variations of A_h and A_θ responses appear to be complex. Additionally, another difference is that two synchronisation regimes are always separated by a desynchronisation region in the type-I regimes for $m^* = 5$ and 20, whereas desynchronisation is not observed for $m^* = 200$. Note that for $m^* = 200$, the foil oscillation frequency responses exhibit all (odd- and even-order) harmonics (i.e. the 1st, 2nd and 3rd harmonics), while the fluid forcing frequency responses display only odd-order harmonics (i.e. the 1st 3rd harmonics), as shown in Fig. 3($c.iii$, $c.iv$). For example, after the oscillations are initially excited, even-order harmonics exhibit some intensities in C_h and C_m until $U^* = 11.8$, which coincides with the location of a local peak of A_h^{10}. These even-order harmonics then vanish after a further increase in U^*. This behaviour persists until $U^* = 13.6$. Beyond this, the even-order harmonics recur in C_h and C_m. In contrast, even-order harmonics are consistently found to be weak in the 2-DOF oscillations, where only odd-order harmonics are observed over the whole U^* range. Such a feature in the frequency PSD contours of C_h and C_m can also be identified from the synchronisation regimes in the cases of $m^* = 5$ or 20. In fact, the fluid forcing frequency responses can be associated with wake modes, as demonstrated by Wang et al. (2020). For the responses induced by

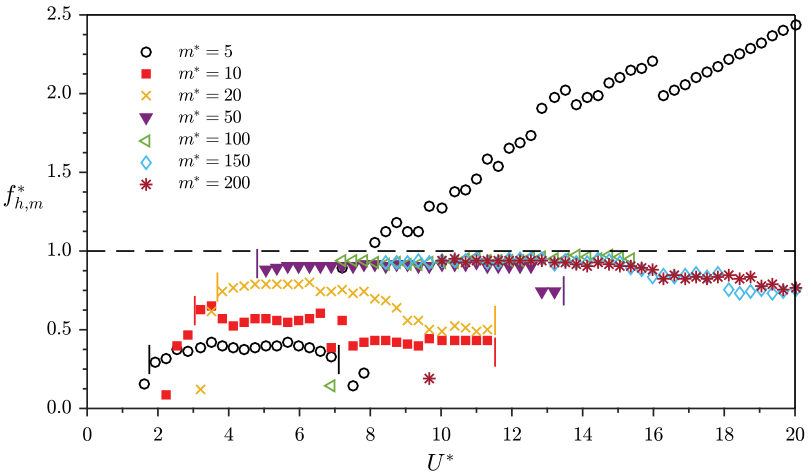

Fig. 8. The main oscillation frequencies in plunge, $f^*_{h,m}$, as a function of U^* at different mass ratios ranging from 5 to 200. The frequencies are normalised by the natural frequency (f_n). The range of type-I regime at each mass ratio is annotated by a pair of short vertical lines.

static instability, the corresponding wake modes are found to shed an odd number of vortices per half oscillation cycle, resulting in an asymmetric forcing that can enhance the body oscillations (see Zhao et al., 2014).

For $x = 0.50$, it can be seen from Fig. 3(b, c) that for both $m^* = 5$ and 20, the dominant oscillation frequencies appear to be fairly constant but much lower than unity over some U^* ranges. To examine the mass ratio effect on the frequency response, Fig. 8 shows the dominant plunging oscillation frequency ($f^*_{h,m}$) as a function of U^* for various mass ratios ranging from 5 to 200. As can be seen, for each mass ratio there exists discrete U^* ranges where $f^*_{h,m}$ is independent of U^*. For example, over the range of $3.9 < U^* < 6.3$ for $m^* = 20$, the oscillation amplitudes are found to increase with U^* and the responses exhibit characteristics similar to those of transverse galloping in 1-DOF FIV systems. Generally, $f^*_{h,m}$ is found to increase with m^* at a fixed U^* location for $m^* \leqslant 50$. This is similar to the galloping-dominated vibrations of a square cylinder studied by Zhao et al. (2019). For $m^* > 50$, $f^*_{h,m}$ gradually approaches unity, consistent with the added mass effect becoming negligible. Moreover, for $m^* \geqslant 5$, multiple U^*-independent frequency response regimes are observed; however, $f^*_{h,m}$ tends to decrease in a higher U^* range, e.g. $f^*_{h,m}$ is observed to be about 0.82 and 0.50 for the ranges of $3.9 < U^* < 6.3$ and $9.8 < U^* < 11.4$, respectively, at $m^* = 20$. This decreasing trend becomes less obvious as m^* is increased. Interestingly, it should be noted that further increases in U^* beyond the type-I regime at a fixed m^* can result in two different types of variation of $f^*_{h,m}$, depending on the mass ratio. For instance, for $m^* \leqslant 5$ (e.g. $m^* = 2$ in Wang et al., 2020), $f^*_{h,m}$ tends to increase linearly with U^* in the high U^* range, as shown in Fig. 8. Such a linear trend indicates that a type-II regime is encountered where the 2-DOF oscillation frequencies are dominated by the vortex shedding frequency.

3.3. Responses with different mass ratios at $x = 0.35$

To further illustrate the combined effect of eccentricity and mass ratio, this subsection discusses the FIV responses at $x = 0.35$, a significant offset from the mass centre of the foil. Fig. 9 shows the amplitude responses as a function of U^* for three different mass ratios of $m^* = 5$, 20 and 200 with fixed $x = 0.35$, and Fig. 10 shows the corresponding frequency PSD contours.

For the cases of $m^* = 5$ and 20 at $x = 0.35$, a type-I regime is firstly encountered upon the onset of significant oscillations, where both A_h and A_θ responses see a sharp rise from zero. This is very similar to the cases at $x = 0.50$. However, for $x = 0.50$, as m^* is increased from 5 to 20, the type-I regime becomes widened, while for $x = 0.35$, the same-type regime is found to shrink. For the type-I regime at both the two pivot locations, synchronisation responses can be identified as the frequency PSD contours exhibit clear harmonics in some U^* ranges, e.g. $4.5 \leqslant U^* \leqslant 5.2$ at $m^* = 5$ as shown in Fig. 10(a).

For both pivot locations investigated, when m^* is increased to 200, the responses exhibit some differences from the results obtained for the other lower mass ratios. For the case of $x = 0.50$ and $m^* = 200$, although the frequency PSD contours display some characteristics similar to the type-I regime, complex variation trends are observed for the amplitude responses. On the other hand, for $x = 0.35$, similar to the cases of lower mass ratios, there are two response regimes observed at $m^* = 200$. In the first regime, significant body oscillations are encountered immediately after the oscillation onset, and the amplitude responses are also found to increase with U^*, as shown in Fig. 9($c.i, c.ii$). However, since the corresponding frequency contours of the first regime in Fig. 10(c) exhibit significant broadband noise, this regime for $m^* = 200$ is also not termed as a type-I regime in the present study. To demonstrate the dynamic characteristics of this

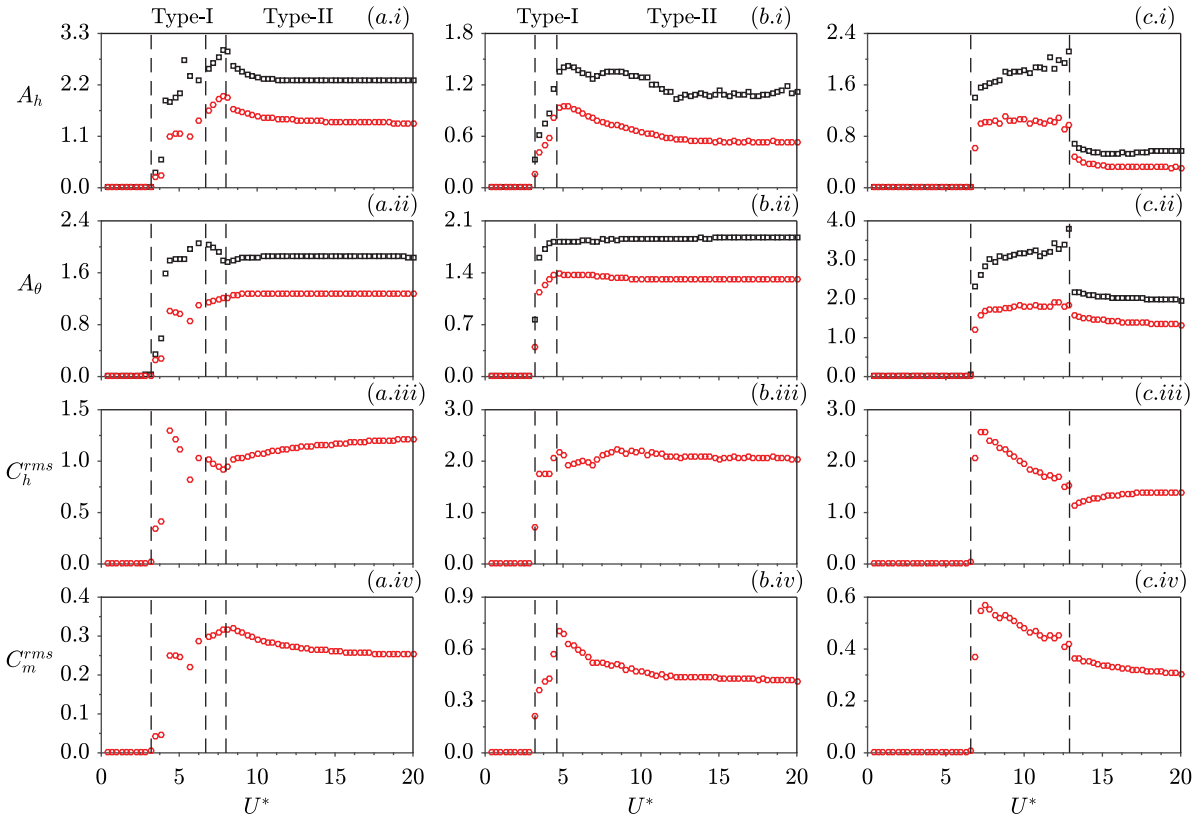

Fig. 9. The normalised response amplitudes at (a) $m^* = 5$, (b) $m^* = 20$ and (c) $m^* = 200$, as a function of U^*, with fixed $x = 0.35$. Further details can be found in the caption of Fig. 2.

regime, Fig. 12(a) shows sample time traces at $U^* = 10.0$ at $m^* = 200$, as a representative for the first regime. The envelope of time profile of the plunge oscillations, as shown in Fig. 12($a.i$), displays a beating behaviour, indicating that two close frequency components may coexist. On the other hand, the time traces of C_h and C_m are found to be highly irregular, which is indicative of a desynchronisation or irregular vortex shedding. These features are not observed for the cases at $x = 0.50$.

It is surprising that the maximum oscillation amplitudes in the first regime for $m^* = 200$ at $x = 0.35$ appear to be noticeably higher than those observed in the type-I regime of the lower mass ratio case of $m^* = 20$. To reveal the mechanism responsible for these unexpected larger amplitudes at a higher mass ratio, Fig. 11 shows the ratios between the r.m.s magnitudes of the three inertial force coefficients, which are induced by the coupling of plunge and pitch, and the fluid forces, as a function of U^* at the three different mass ratios of $m^* = 5$, 20 and 200. The three coefficient ratios are denoted by r_{Ih}^A, r_{Ih}^C and $r_{I\theta}$, given by Eqs. (6)–(8), respectively. Interestingly, the three coefficient ratios appear to be much higher in the first regime for $m^* = 200$ than other regimes. For $m^* = 200$, the three coefficient ratios are found to reach their peak values when the oscillations are initially encountered at $U^* = 6.7$, and then decrease as U^* varies. The peak values of r_{Ih}^C and $r_{I\theta}$ are both higher than 1.0, indicating that the corresponding inertial forces are even stronger than the fluid forces. When U^* is further increased beyond the first regime, the oscillation amplitudes see rapid drops, as shown in Fig. 9(c). Meanwhile, all the three coefficient ratios seem to approach a plateau at high reduced velocities. Therefore, significantly large oscillation amplitudes at $m^* = 200$ could be attributed to the much stronger inertial forces associated with this eccentricity.

As U^* is further increased beyond the first regime for all the three mass ratios, the oscillation amplitudes gradually reach plateaus at high reduced velocities, while, on the other hand, the oscillation frequencies increase in a linear relationship with U^*. This indicates the formation of a type-II regime. At $x = 0.35$, the type-II response appears for all mass ratios, whereas it is only observed for the lowest m^* tested in the present study, i.e. $m^* = 5$, at $x = 0.5$. This suggests that the existence of a type-II regime is strongly dependent on the eccentricity effect. Specifically, for $m^* = 20$, the type-II response is found over the range of $5.5 \leqslant U^* \leqslant 20.0$, where the frequency response displays some broadband noise, as shown in Fig. 10(b). Another important feature of the type-II response at $m^* = 20$ is that each harmonic seems to have one accompanying component at least, with a frequency close to the harmonic. This can often result in beating patterns in the time varying amplitude time traces. For instance, the normalised frequency difference between the harmonics and

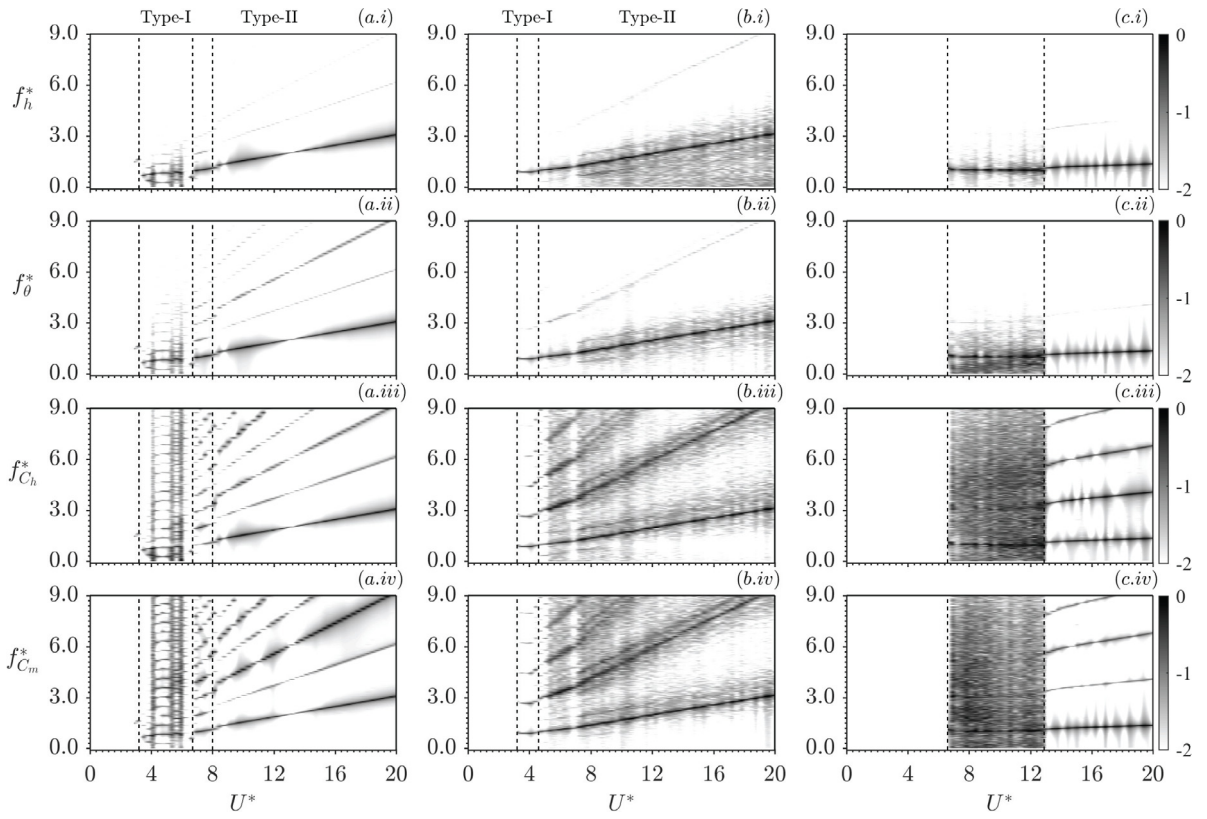

Fig. 10. The logarithmic-scale frequency PSD contours as a function of U^* for (a) $m^* = 5$, (b) $m^* = 20$ and (c) $m^* = 200$ with fixed $x = 0.35$. Further details can be found in the caption of Fig. 3.

their accompanying components for the plunging oscillations, denoted by Δf_{har}^*, are found to be approximately 0.62. To further demonstrate this characteristic, sample time traces of the response at $U^* = 10.39$ with $m^* = 20$ are plotted in Fig. 12(b), showing that the time traces exhibit quasi-periodic and beating patterns. Similar behaviour is also observed in the type-I regime of $m^* = 200$, as shown in Fig. 12($b.i$). In fact, such a beating feature is found to widely exist in the responses with fixed $x = 0.35$ for high m^* values (i.e. $m^* > 5$ in the present study).

Fig. 13 shows sample time traces of the normalised plunge displacement for various mass ratios ($m^* = 75$, 105, 125 and 155) at $U^* = 8.0$. Clearly, all cases display beating behaviour, and the beating patterns seem to be affected significantly by m^*. In Fig. 13(a), the beating pattern appears to be periodic and well-modulated by two strong frequency components. Nevertheless, such a periodic pattern becomes weaker gradually as m^* is increased; e.g., the time trace in Fig. 13(d) is found to be aperiodic and chaotic. As mentioned previously in Section 3.2, increasing the mass ratio could help to suppress the chaotic behaviours when the pivot location is close to the mass centre and thereby the eccentricity effect is insignificant. On the contrary, when the eccentricity plays a significant role in the response, i.e. at $x = 0.35$ in the present case, increasing the mass ratio would result in a much stronger inertial coupling and thus enhance the chaotic dynamics.

3.4. Responses as a function of m^*

From the results discussed above at the three different mass ratios, the variation of the mass ratio can result in distinctly different response behaviours, especially when the pivot location is of significant offset from the mass centre. To further demonstrate the effect of mass ratio, the 2-DOF amplitude responses are examined as a function of m^* at the two fixed pivot locations $x = 0.35$ and 0.50. Fig. 14 shows the amplitude responses for four different combinations of x and U^*, which are selected as representatives for the type-I and type-II regimes at each pivot location.

For $x = 0.35$ shown in Fig. 14(a), where the eccentricity plays a significant role, increasing m^* does not necessarily attenuate the foil oscillations. Interestingly, for a very high m^* (i.e. $m^* \geqslant 200$) at a fixed U^*, the oscillation amplitudes are observed to be fairly stable, and further increases in m^* do not seem to have any significant effect on the amplitude responses. However, $m^* = 75$ appears to be a critical value for $(x, U^*) = (0.35, 8.0)$, at which a sudden jump is encountered in both A_h^{10} and A_θ^{10} responses at $m^* = 75$, as shown in Fig. 14(a). For $m^* < 75$, A_θ^{10} is found to increase linearly

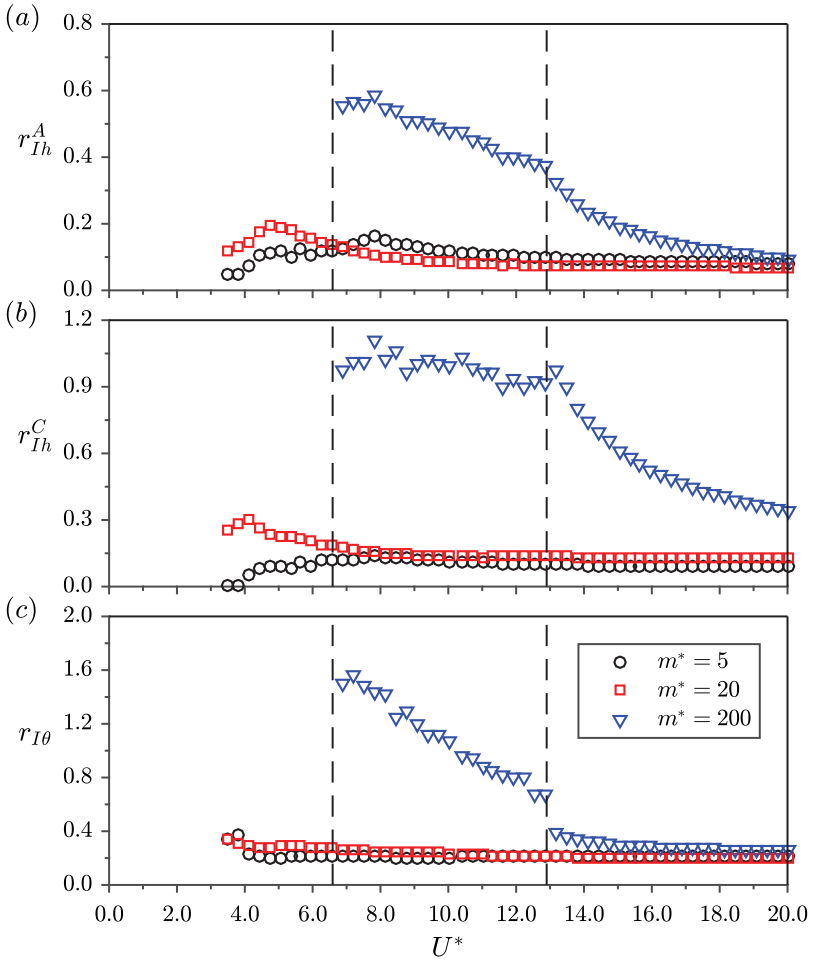

Fig. 11. Comparisons of three coefficient ratios (a) r^A_{Ih}, (b) r^C_{Ih}, and (c) $r_{I\theta}$ as a function of U^* for three different mass ratios of $m^* = 5$, 20 and 200, with fixed $x = 0.35$. The response regime with unexpected oscillation amplitudes at $m^* = 200$ is annotated by the dash lines.

with m^*, while the reverse trend is observed for A^{10}_h. On the other hand, for $m^* \geqslant 75$, a stable A^{10}_θ response is achieved, while the A^{10}_h response sees a slow decrease as m^* is increased. This implies changes in the dynamic characteristics that are associated with violent oscillations or unexpected amplitudes in the type-I regime at high mass ratios (e.g. $m^* = 200$). In addition, the comparisons of r^A_{Ih}, r^C_{Ih} and $r_{I\theta}$ in Fig. 11 suggest that such changes in the dynamic characteristics are well related to the inertial forces induced by the coupling of plunge and pitch oscillations. To demonstrate this, Fig. 15(*a*, *b*) show the variations of r^A_{Ih}, r^C_{Ih} and $r_{I\theta}$ as a function of m^* for $U^* = 8.0$ and 16.0, respectively, with $x = 0.35$. Note that these two U^* values are selected as representatives of the first and second regimes at $m^* = 200$, respectively. It is interesting to note that, in the range of $m^* < 75$ with $(x, U^*) = (0.35, 8.0)$, $r_{I\theta}$ exhibits very minor variations with m^*, prior to an increasing trend for $m^* \geqslant 75$, as shown in Fig. 15(*a*). However, such a jump in the oscillation amplitude responses at $U^* = 8.0$ are not observed at $U^* = 16.0$, as demonstrated in Fig. 14(*b*). In contrast, Fig. 15(*b*) shows that $r_{I\theta}$ at $U^* = 16.0$ reaches a local peak at $m^* = 55$ and then decreases as m^* is further increased.

For the case of $x = 0.5$, where $b = 0.04$ is close to zero, it can be seen that the eccentricity effect on the FIV response is insignificant. Thus, similar to many other 1-DOF bluff body systems, increasing m^* in this case can significantly attenuate (in most situations) and even suppress the amplitude responses at a given U^*, as demonstrated in Fig. 14(*c*, *d*). Additionally, the present study finds that there exists a critical mass ratio, m^*_c, above which the 2-DOF oscillations are suddenly suppressed. The observed critical mass ratios for the two U^* locations are illustrated in Fig. 14(*c*, *d*): m^*_c is found to be 100 and 260 for $U^* = 7.0$ and 11.0, respectively. It seems that m^*_c tends to increase with U^* at $x = 0.5$.

3.5. Responses as a function of x

To further assess the effect of eccentricity, the oscillation responses as a function of x at a fixed combination of m^* and U^* are discussed in this subsection, where x is examined in the range of $0.1 \leqslant x \leqslant 0.88$, with a resolution of 0.025, while

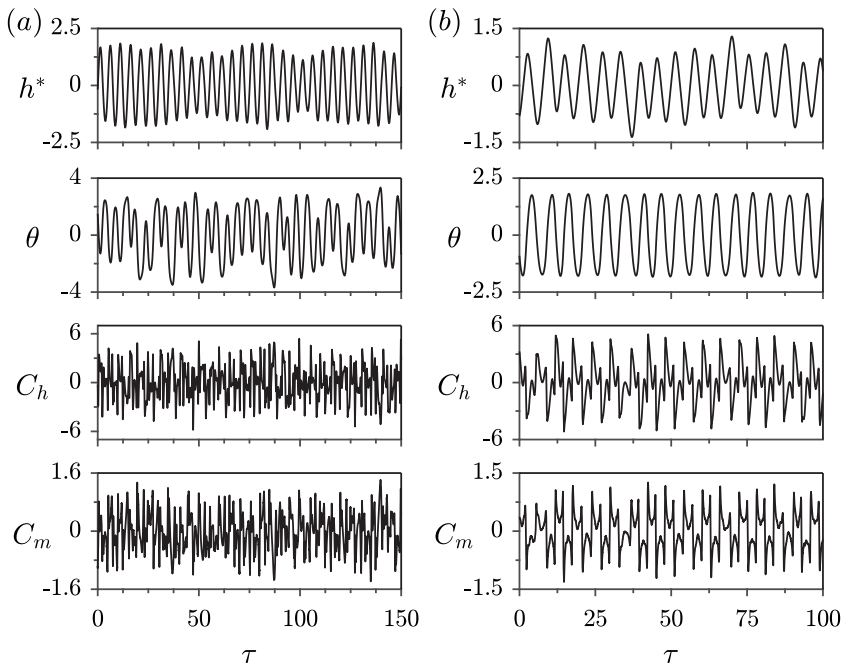

Fig. 12. Time traces of the responses at (a) $(m^*, U^*) = (200, 10.0)$ and (b)$(m^*, U^*) = (20, 10.39)$, with fixed $x = 0.35$. Further details can be found in the caption of Fig. 4.

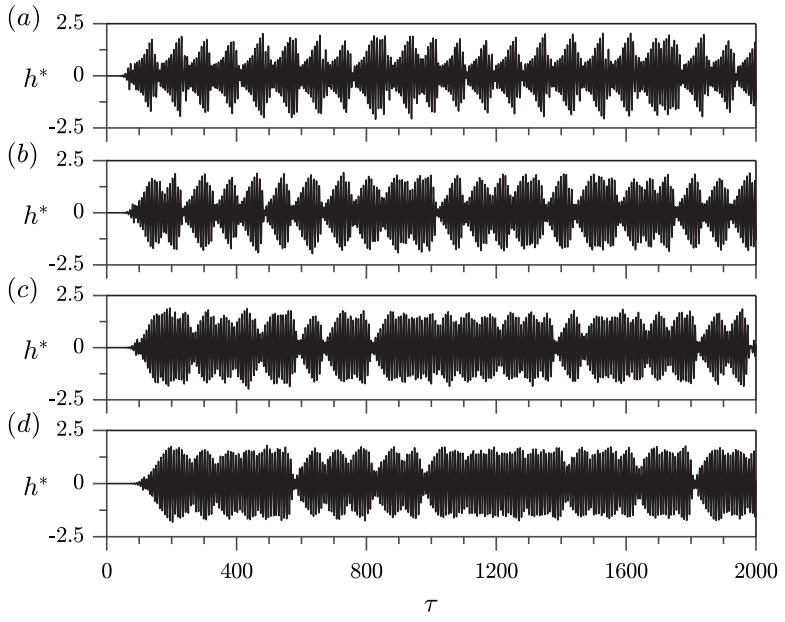

Fig. 13. Time traces of the normalised displacements in plunge with a beat characteristic at (a) $m^* = 75$, (b) $m^* = 105$, (c) $m^* = 125$ and (d) $m^* = 155$, with $U^* = 8.0$ and $x = 0.35$.

the mass centre remains at $x = 0.46$. As previous results have shown that the eccentricity effect becomes more obvious at high mass ratio, the mass ratio is thereby set to be 200. The reduced velocity is 10.0 as a representative of the first response regime for $(x, m^*) = (0.35, 200)$, where significant foil oscillations are encountered.

Fig. 16 shows: (*a*) the A_h^{10} and A_θ^{10} responses; and (*b*) the ratios of fluid forcing coefficient magnitudes as a function of x. As can be seen, significant oscillation amplitudes are observed within two ranges: $0.25 \leqslant x \leqslant 0.425$ and $0.5 \leqslant x \leqslant 0.675$, while at other locations (including those close to the leading edge, trailing edges and mass centre) oscillations are found to be negligible. As mentioned previously in Section 3.1, *static instability* is responsible for the generation of oscillations

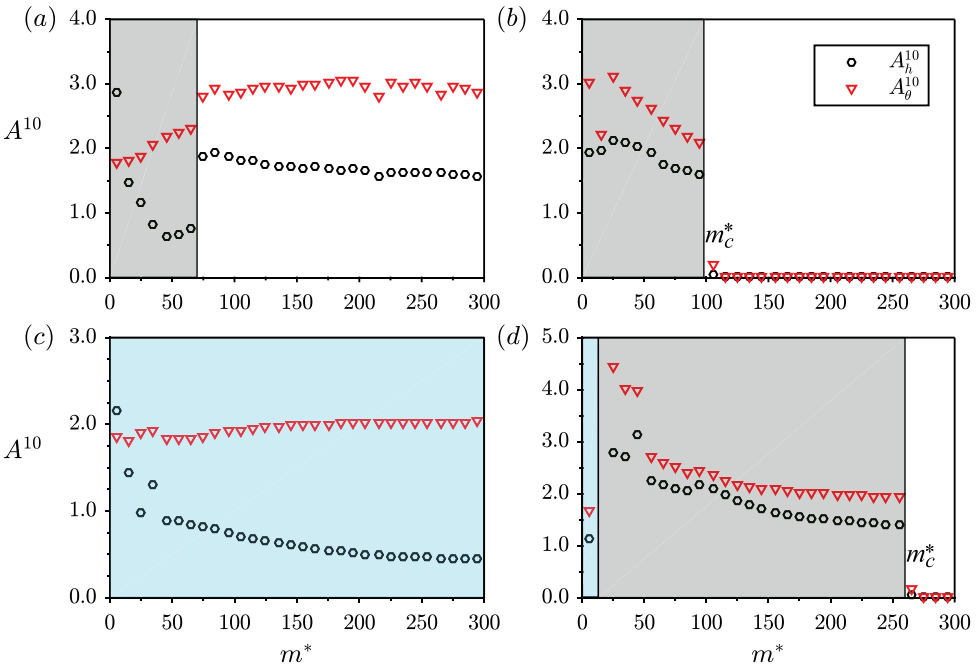

Fig. 14. A_h^{10} and A_θ^{10} as a function of m^* at four fixed combinations of x and U^*: (a) $x = 0.35$ and $U^* = 8.0$, (b) $x = 0.50$ and $U^* = 7.0$, (c) $x = 0.35$ and $U^* = 16.0$, $m_c^* = 100$ and (d) $x = 0.50$ and $U^* = 11.0$, $m_c^* = 260$. The type-I and type-II responses are highlighted by the grey and blue areas, respectively. Note that m_c^* denotes the critical mass ratio, above which the oscillations are suppressed. (For interpretation of the references to colour in this figure legend, the reader is referred to the web version of this article.)

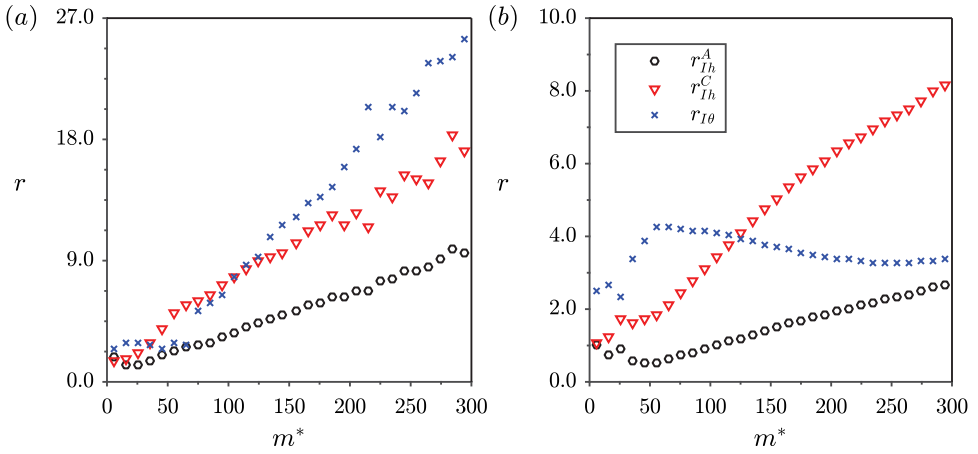

Fig. 15. The coefficient ratios of r_{Ih}^A, r_{Ih}^C and $r_{I\theta}$ as a function of m^* at $x = 0.35$ with (a) $U^* = 8.0$ and (b) $U^* = 16.0$.

in the present study, which can also be confirmed from the amplitude responses at $x = 0.25$ in Fig. 16(a). Following the derivation given by Dowell (2015), the critical speed for the onset of static instability can be determined by

$$qSe\frac{\partial C_h}{\partial \theta} - k_\theta = 0, \tag{16}$$

where q is the critical dynamic pressure, S is the area of the foil, and e is the distance between the aerodynamic centre and the pivot location, which is positive if the aerodynamic centre is ahead of the pivot location. For a foil placed in a two-dimensional incompressible flow, its aerodynamic centre is located at the quarter chord. For a foil with zero angle of attack, $\partial C_h/\partial\theta$ is a positive value. Therefore, with q, S and k_θ being positive, Eq. (16) fails if e becomes negative. This suggests that static instability will not be observed below $x = 0.25$. The variations of A_h^{10} and A_θ^{10} with x in Fig. 16(a) illustrate that the effect of the pivot location is nonlinear. For example, both A_h^{10} and A_θ^{10} are observed to be zero at $x = 0.45$, while violent oscillations can be seen at other adjacent locations, e.g. $x = 0.425$. In addition, rapid drops

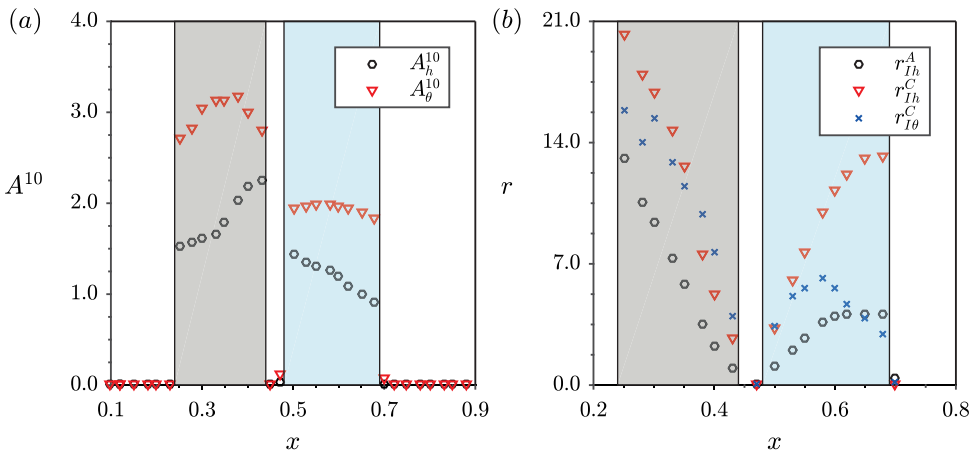

Fig. 16. (a) A_h^{10} and A_θ^{10}, and (b) r_{Ih}^A, r_{Ih}^C and $r_{I\theta}$, as a function of x at $m^* = 200$ and $U^* = 10.0$. Regimes with oscillations are highlighted by the areas with colours. (For interpretation of the references to colour in this figure legend, the reader is referred to the web version of this article.)

observed in both A_h^{10} and A_θ^{10} at $x = 0.25$ and 0.675 also suggest that the responses could be sensitive to the pivot location. Moreover, the overall A_h^{10} and A_θ^{10} responses over the range of $0.5 \leqslant x \leqslant 0.675$ appear to be lower than those in the range of $0.25 \leqslant x \leqslant 0.43$.

If the pivot location is moved from the mass centre to either of the two edges with other parameters fixed, A_θ^{10} is firstly observed to reach a local peak and then decrease, while A_h^{10} shows a reversed relation with x, as can be observed from Fig. 16(a). On the other hand, a larger distance between the pivot location to the mass centre can also result in higher r_{Ih}^A, r_{Ih}^C, indicating a stronger inertial effect in plunging induced by pitching. Note that if the pivot location is moved towards the leading edge, the inertial effect in pitching will also be enhanced, as $r_{I\theta}$ is also observed to become larger. However, if the pivot location is moved towards the trailing edge, $r_{I\theta}$ sees its maximum at $x = 0.575$ and starts to decrease with the oscillation amplitudes, suggesting that the inertial effect becomes weak in pitch for this situation. The decrease of $r_{I\theta}$ also limits the increase of r_{Ih}^A and r_{Ih}^C and the foil is found to be stationary after x becomes higher than 0.675. Interestingly, as shown in Fig. 16, when A_θ^{10} reaches a local peak on one side of the mass centre, a variation can also be observed for r_{Ih}^C. For example, on the left side of the mass centre, the variation curves of r_{Ih}^C and $r_{I\theta}$ intersect around $x = 0.375$, where r_{Ih}^C is observed to be larger than $r_{I\theta}$ and A_θ^{10}, then starts to decrease from its peak as the pivot location is moved towards the leading edge. On the other hand, on the right side of the mass centre, a local peak can be seen for $r_{I\theta}$ at $x = 0.58$. The correlation between the oscillation amplitudes and the inertial forces indicates that the competition between the inertial forces associated with the eccentricity can play an important role affecting the oscillation responses.

4. Conclusions

In the present study, effects of the eccentricity and mass ratio have been studied for a foil undergoing fully passive oscillations of plunge and pitch in a two-dimensional incompressible flow at $Re = 400$, by employing an immersed boundary method.

The analysis shows that two types of FIV responses, labelled as type-I and type-II, can be identified for low mass ratios for two fixed pivot locations, $x = 0.5$ and 0.35, where the eccentricity effect plays an insignificant and a significant role, respectively. The type-I regime, which is driven by static instability, is mainly observed at low reduced velocities. In a type-I regime, the oscillation amplitudes are found to increase with U^* in most situations and the dominant oscillation frequencies exhibit slight dependences on U^* in some specific U^* ranges. Harmonic synchronisation responses are encountered in some U^* ranges, e.g. $6.28 \leqslant U^* \leqslant 7.52$ at $m^* = 20$ and $x = 0.50$. On the other hand, a type-II response is often encountered at high U^* for the present two pivot locations, where the oscillation and fluid forcing frequencies tend to increase with U^*, while the oscillation amplitudes are fairly stable in the response regime.

In cases where the eccentricity effect is insignificant, i.e. at $x = 0.5$ close to the foil's mass centre ($x = 0.46$), the type-I regime widens as m^* is increased in a low mass ratio range, e.g. $5 \leqslant m^* \leqslant 20$. However, when m^* is increased to large values, e.g. $m^* \geqslant 200$, the frequency response only exhibits characteristics of the type-I response, while the amplitude responses are found to be complex, with synchronisation responses observed regardless of U^*. On the other hand, a type-II response can only be observed at low m^*. In addition, increasing the mass ratio favours suppression of chaotic responses. Interestingly, it is found from the FIV responses as a function of m^* at $x = 0.5$ that, for a fixed reduced velocity, there exists a critical mass ratio, above which the foil oscillations will suddenly be suppressed. The critical mass ratio tends to increase with increased reduced velocity.

In cases where the eccentricity effect is significant, i.e. at $x = 0.35$, the type-I regime is found to shrink as m^* is increased in the low range. Further increase in m^* can result in chaotic responses with violent oscillations in a lower U^* range, where the inertial forces induced by the coupling between plunge and pitch play a significant role affecting the dynamics. In addition, the amplitude responses as a function of m^* with fixed $x = 0.35$ indicate that the oscillation amplitudes become stable as m^* is increased above a certain value.

Furthermore, the present study also confirms the occurrence of static instability as well as the nonlinear effect of eccentricity. From the responses as a function of the pivot location, with fixed m^* and U^*, it is found that when the pivot location is moved close to either of the two edges, violent oscillations could suddenly be suppressed, while a small change in the distance between the pivot location and the mass centre could result in violent oscillations. Moreover, the foil experiences much more violent oscillations if the pivot location is moved towards the leading edge rather than the trailing edge.

Analysis of the response dynamics in this work should be helpful for the parameter design of flow energy extraction of 2-DOF flapping foils. Note that, higher oscillation amplitudes do not necessarily result in a better efficiency. Synchronisation responses, with a good periodicity and optimal pitch-to-plunge phase ($\sim 90^\circ$) occurring around $x = 0.35$, are preferable for the flow energy extraction. The present numerical study shows that the combined effects of eccentricity and mass ratio can result in profound FIV phenomena for a foil subject to two degrees of freedom of plunge and pitch. Thus, it would be of interest to investigate and confirm the observed effects in future experiments.

Declaration of competing interest

The authors declare that they have no known competing financial interests or personal relationships that could have appeared to influence the work reported in this paper.

Acknowledgements

The authors gratefully acknowledge the financial support from the National Science Foundation of China grants 51790514 and 52022009, National Science and Technology Major Project grants 2017-II-0009-0023 and 2017-II-003-0015, and the Academic Excellence Foundation of BUAA for PhD Students. In addition, J.Z. and M.C.T. acknowledge the financial support through the Australian Research Council (ARC) Discovery Project grant DP170100275, and J.Z. also acknowledges the support for his research fellowship through the ARC Discovery Early Career Research Award scheme DE200101650.

References

Ashraf, M.A., Young, J., S. Lai, J.C., 2011. Numerical analysis of an oscillating-wing wind and hydropower generator. AIAA J. 49 (7), 1374–1386.
Bearman, P.W., 1984. Vortex shedding from oscillating bodies. Annu. Rev. Fluid Mech. 195–222.
Blevins, R.D., 1990. Flow-Induced Vibration, second ed. Krieger.
Boudreau, M., Dumas, G., Rahimpour, M., Oshkai, P., 2018. Experimental investigation of the energy extraction by a fully-passive flapping-foil hydrokinetic turbine prototype. J. Fluids Struct. 82, 446–472.
Boudreau, M., Gunther, K., Dumas, G., 2019a. Free-pitching flapping-foil turbines with imposed sinusoidal heave. J. Fluids Struct. 90, 110–138.
Boudreau, M., Gunther, K., Dumas, G., 2019b. Investigation of the energy-extraction regime of a novel semi-passive flapping-foil turbine concept with a prescribed heave motion and a passive pitch motion. J. Fluids Struct. 84, 368–390.
Boudreau, M., Picard-deland, M., Dumas, G., 2020. A parametric study and optimization of the fully-passive flapping-foil turbine at high Reynolds number. Renew. Energy 146, 1958–1975.
Crawford, J.D., Knobloch, E., 1991. Symmetry and symmetry-breaking bifurcations in fluid dynamics. Annu. Rev. Fluid Mech. 23 (1), 341–387.
Deng, J., Teng, L., Pan, D., Shao, X., 2015. Inertial effects of the semi-passive flapping foil on its energy extraction efficiency. Phys. Fluids 27 (5).
Dowell, E.H., 2015. A Modern Course in Aeroelasticity, fifth ed. Springer International Publishing, Switzerland.
Du, L., Sun, X., Yang, V., 2016a. Generation of vortex lift through reduction of rotor/stator gap in turbomachinery. J. Propul. Power 32 (2), 472–485.
Du, L., Sun, X., Yang, V., 2016b. Vortex-lift mechanism in axial turbomachinery with periodically pitched stators. J. Propul. Power 32 (2), 1–14.
Duarte, L., Dellinger, N., Dellinger, G., 2019. Experimental investigation of the dynamic behaviour of a fully passive flapping foil hydrokinetic turbine. J. Fluids Struct. 88, 1–12.
Feng, C.C., 1968. The Measurement of Vortex Induced Effects in Flow Past Stationary and Oscillating Circular and D-Section Cylinders (Masters). (October), The University of British Columbia.
Gabbai, R., Benaroya, H., 2005. An overview of modeling and experiments of vortex-induced vibration of circular cylinders. J. Sound Vib. 282 (3), 575–616.
Govardhan, R., Williamson, C.H.K., 2000. Modes of vortex formation and frequency response of a freely vibrating cylinder. J. Fluid Mech. 420 (2000), 85–130.
Govardhan, R., Williamson, C.H.K., 2002. Resonance forever: existence of a critical mass and an infinite regime of resonance in vortex-induced vibration. J. Fluid Mech. 473 (2002), 147–166.
Griffin, O.M., Skop, R.A., Koopmann, G.H., 1973. The vortex-excited resonant vibrations of circular cylinders. J. Sound Vib. 31 (2), 235–249.
Jauvtis, N., Williamson, C.H.K., 2004. The effect of two degrees of freedom on vortex-induced vibration at low mass and damping. J. Fluid Mech. 509 (509), 23–62.
Khalak, A., Williamson, C.H.K., 1996. Dynamics of a hydroelastic cylinder with very low mass and damping. J. Fluids Struct. 10 (5), 455–472.
Kinsey, T., Dumas, G., 2008. Parametric study of an oscillating airfoil in a power-extraction regime. AIAA J. 46 (6), 1318–1330.
Leontini, J.S., Thompson, M.C., 2013. Vortex-induced vibrations of a diamond cross-section: sensitivity to corner sharpness. J. Fluids Struct. 39, 371–390.
McKinney, W., DeLaurier, J., 1981. The wingmill: an oscillating-wing windmill. J. Energy 5 (2), 109–115.
Morse, T.L., Williamson, C.H.K., 2009. Prediction of vortex-induced vibration response by employing controlled motion. J. Fluid Mech. 634, 5–39.
Naudascher, E., Rockwell, D., 2005. Flow-Induced Vibrations: An Engineering Guide. Dover Publications.

Nemes, A., Zhao, J., Lo Jacono, D., Sheridan, J., 2012. The interaction between flow-induced vibration mechanisms of a square cylinder with varying angles of attack. J. Fluid Mech. 710, 102–130.
Paidoussis, M.P., Price, S.J., De Langre, E., 2010. Fluid Structure Interactions: Cross-Flow-Induced Instabilities. Cambridge University Press.
Peskin, C.S., 1972. Flow patterns around heart valves: a numerical method. J. Comput. Phys. 10 (2), 252–271.
Peskin, C.S., 1977. Numerical analysis of blood flow in the heart. J. Comput. Phys. 25 (3), 220–252.
Peskin, C.S., 2002. The immersed boundary method. Acta Numer. 11, 479–517.
Platzer, M., Ashraf, M., Young, J., Lai, J., 2010. Extracting power in jet streams: Pushing the performance of flapping-wing technology. In: 27th International Congress of the Aeronautical Sciences, Nice, France. pp. 19–24.
Sarpkaya, T., 2004. A critical review of the intrinsic nature of vortex-induced vibrations. J. Fluids Struct. 19 (4), 389–447.
Seyed-Aghazadeh, B., Carlson, D.W., Modarres-Sadeghi, Y., 2017. Vortex-induced vibration and galloping of prisms with triangular cross-sections. J. Fluid Mech. 817 (May), 590–618.
Soti, A.K., Zhao, J., Thompson, M.C., Sheridan, J., Bhardwaj, R., 2018. Damping effects on vortex-induced vibration of a circular cylinder and implications for power extraction. J. Fluids Struct. 81, 289–308.
Veilleux, J.C., Dumas, G., 2017. Numerical optimization of a fully-passive flapping-airfoil turbine. J. Fluids Struct. 70, 102–130.
Wang, Z., Du, L., Zhao, J., Sun, X., 2017. Structural response and energy extraction of a fully passive flapping foil. J. Fluids Struct. 72, 96–113.
Wang, Z., Du, L., Zhao, J., Thompson, M., Sun, X., 2020. Flow-induced vibrations of a pitching and plunging airfoil. J. Fluid Mech. 885, A36.
Williamson, C.H.K., Govardhan, R., 2004. Vortex-induced vibrations. Annu. Rev. Fluid Mech. 36 (1), 413–455.
Williamson, C.H., Roshko, A., 1988. Vortex formation in the wake of an oscillating cylinder. J. Fluids Struct. 2 (4), 355–381.
Xiao, Q., Zhu, Q., 2014. A review on flow energy harvesters based on flapping foils. J. Fluids Struct. 46, 174–191.
Young, J., Lai, J.C., Platzer, M.F., 2014. A review of progress and challenges in flapping foil power generation. Prog. Aerosp. Sci. 67, 2–28.
Zhao, J., Hourigan, K., Thompson, M.C., 2018a. Flow-induced vibration of D-section cylinders: an afterbody is not essential for vortex-induced vibration. J. Fluid Mech. 851, 317–343.
Zhao, J., Leontini, J.S., Lo Jacono, D., Sheridan, J., 2014. Fluid–structure interaction of a square cylinder at different angles of attack. J. Fluid Mech. 747, 688–721.
Zhao, J., Leontini, J.S., Lo Jacono, D., Sheridan, J., 2019. The effect of mass ratio on the structural response of a freely vibrating square cylinder oriented at different angles of attack. J. Fluids Struct. 86, 200–212.
Zhao, J., Nemes, A., Lo Jacono, D., Sheridan, J., 2018b. Branch/mode competition in the flow-induced vibration of a square cylinder. Philos. Trans. R. Soc. Lond. Ser. A 376, 20170243.
Zhu, Q., 2012. Energy harvesting by a purely passive flapping foil from shear flows. J. Fluids Struct. 34, 157–169.